Circularizing Rydberg atoms with time-dependent optical traps

Ryan Cardman ●* and Georg Raithel ●
Department of Physics, University of Michigan, Ann Arbor, Michigan 48105, USA

We discuss three proposed schemes of initializing circular-state Rydberg atoms via optical couplings provided by the ponderomotive effect in contrast to the current circularization methods that utilize electric-dipole interactions. In our first proposed method, a radial optical trap consisting of two Laguerre-Gaussian beams of opposite winding numbers transfers orbital angular momentum to the Rydberg atom, providing a first-order coherent coupling between an F state and a circular state. Additionally, we propose a one-dimensional ponderomotive optical lattice modulated at rf frequencies, providing quadrupolelike couplings in the hydrogenic manifold for rapid adiabatic passage through a series of intermediate Rydberg states into the circular state. For the third proposed scheme, a two-dimensional ponderomotive optical lattice with a time-orbiting trap center induces effectively the same coupling as a σ^+- or σ^--polarized rf field of tunable purity for all-optical rapid adiabatic passage into the circular state.

I. INTRODUCTION

Circular-state (CS) Rydberg atoms have maximum orbital angular momenta and reside in the extreme Zeeman sublevels. Electric-dipole selection rules permit spontaneous emission solely between adjacent CSs, extending lifetimes to the order of ms. Because of this feature allowing sufficient time for making spectroscopic measurements, CS Rydberg atoms are desirable for cavity QED experiments [1] and high-precision spectroscopy [2]. Examples of two ongoing experiments consist of a linear chain of trapped CS Rydberg atoms experiencing dipole-dipole and van der Waals interactions for quantum simulation [3] and a precise measurement of the Rydberg constant for solving the proton radius puzzle [2,4].

Because plane-wave electromagnetic fields change the internal angular momentum to an atom by only up to one $\hbar$ (in first order), one cannot use standard laser excitation to prepare a sample of CS Rydberg atoms, which usually have $\simeq 20\hbar$ units of orbital angular momentum or more. Two popular methods of circularization are the crossed-fields method [5–8] and the rapid adiabatic passage (RAP) method [9–11]. In the crossed-fields method, perpendicular electric and magnetic fields with slowly varying amplitudes are applied to the system to adiabatically switch atoms in a low-$|m_l|$ state into the CS. The initial field magnitudes are chosen such that the Stark splitting is much larger than that of the Zeeman interaction. With this initial configuration, the outermost levels of the hydrogenic manifold are Stark states with $m_l \simeq 0$ and are accessible by laser excitation. As the electric field is adiabatically switched off, while the transverse magnetic field remains fixed or adiabatically increases, the fields transfer the atom to the CS. While this is an effective method, it requires efficient suppression of electric-field noise. In the RAP method with linearly polarized radiation, rf waves couple states with

low magnetic quantum numbers $|m_l| \leqslant 3$ to the CS. In this scheme, the electric and magnetic fields are parallel and lift the degeneracy of the hydrogenic states. For rf waves of a chosen frequency, the relevant dressed states nearly cross at a specified electric field. Electric-dipole coupling induced by an rf field turns this crossing into a multilevel avoided crossing, which permits adiabatic switching of the atoms from a low-angular-momentum state, accessible by lasers, to the CS via scanning of the electric field. Applications which require parallel electric and magnetic fields or a quantization axis defined by the Stark interaction find the RAP method more favorable than the crossed-fields method [2,11], for the latter would require diabatic switching of the atoms into the Stark-dominated regime by a sudden turn-on of an electric field parallel to the magnetic field subsequent to the circularization [11].

The aforementioned methods employ slowly varying perturbations to the atomic system for efficient circularization; however, there has been recent interest in fast transitions into the CS with purely σ^+-polarized rf fields [12]. Simulations based on quantum optimal control theory can be performed to choose rf fields with appropriate relative phases and amplitudes to optimize the speed of circularization [13]. In such methods, multiple hydrogenic states are excited at once, making the process analogous to a transition from one coherent state to another.

The quantum dynamics of the methods discussed arise from the term proportional to $\mathbf{A} \cdot \mathbf{p}$ in the minimal coupling Hamiltonian for a charged particle. This term describes electric-multipole transitions and the Stark effect. The term proportional to A^2 describes the diamagnetic and ponderomotive shifts (e.g., the Kapitza-Dirac effect in electrons [14,15]). In Rydberg atoms with weakly bound valence electrons, a rapidly oscillating electric field pushes the Rydberg electron to regions of intensity minima by means of the ponderomotive interaction [16], thereby exerting a net force on the entire atom. Therefore, this term becomes significant when dealing

*rcardman@umich.edu

with Rydberg atoms. In this paper, we discuss methods of circularization involving ponderomotive interactions of the Rydberg electron, which are due to the A^2 part of the minimal coupling Hamiltonian.

Hermite-Gaussian (HG) modes of electromagnetic waves contain single units of angular momentum, whereas a properly prepared Laguerre-Gaussian (LG) mode of winding number m has an angular momentum of $m\hbar$ per photon that can be on the order of a CS Rydberg atom's angular momentum. In Sec. II of this paper, we propose a method of coherent Rydberg atom circularization with two copropagating LG beams of winding numbers with the same magnitude $|m|$ but opposite signs. If the wavelengths of the beams are chosen appropriately, inelastic, coherent scattering between the modes, effected by the ponderomotive interaction, enables direct coupling of a low-m_l Rydberg level with the CS. Multipole interactions of LG modes and Rydberg atoms have been discussed, where matrix elements coupling low-angular momentum states to high-angular momentum hydrogenic states were calculated [17,18], but these methods differ from ours, as they involve electric-multipole transitions due to the $\mathbf{A} \cdot \mathbf{p}$ term, not ponderomotive interactions.

In Sec. III, we discuss an optically based RAP scheme that involves electric-quadrupole-equivalent coupling between Stark states of different m_l by means of an rf-modulated ponderomotive optical lattice (POL) [19,20]. This proposed scheme also allows the atoms to remain trapped during the circularization, does not require rf fields in the atom-field interaction region, and enables circularization of atoms with a spatial selectivity on the order of μm.

In Sec. IV, we discuss atoms in a two-dimensional POL with its trap center modulated in a circular motion at rf frequencies, analogous to the TOP trap used for Bose-Einstein condensation [21]. The resulting ponderomotive interaction has the same effect as electric-dipole couplings by a purely σ^+- or σ^--polarized rf field. Circularization schemes using this time-orbiting ponderomotive optical lattice (TOPOL) are more efficient than RAP schemes with linearly polarized rf radiation by preventing "leakage" transitions [9–11].
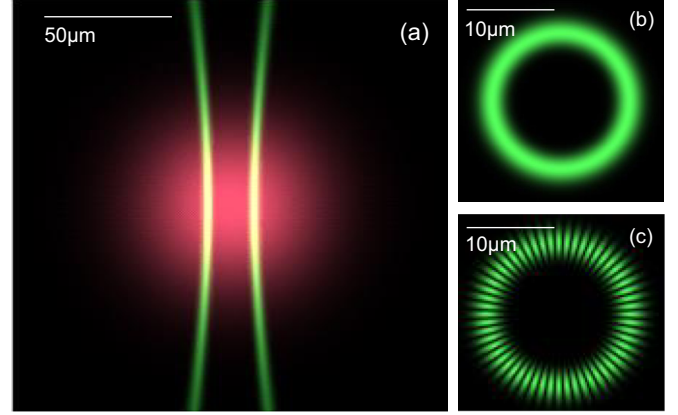

FIG. 1. For all figures above, $m = 14$. In (a), the longitudinal intensity profile of the two superimposed beams with $\lambda_1 = 536$ nm and $\lambda_2 = 532$ nm is shown as they overlap a cloud of ultracold ^{85}Rb. The diameter of a 21F Rydberg atom and $n = 32$ CS are at the order of a hundredth of the beam's diameter at $z = 0$. In (b), the time-independent part of the ponderomotive potential $V_p(\mathbf{r})$ is plotted at $z = 0$; in (c), we show the magnitude of the time-dependent part of the ponderomotive potential V_C on the xy-plane for $t = 0$.

In Sec. V, we discuss the advantages and disadvantages of our proposed all-optical schemes in comparison to the previously proposed and demonstrated nonoptical methods.

II. CIRCULARIZATION BY LAGUERRE-GAUSSIAN LASER MODES

A. Theoretical model

Consider a coherent superposition of two LG modes (1 and 2), with respective field amplitudes $\mathcal{E}_1$ and $\mathcal{E}_2$, respective winding numbers $-m$ and m, and respective angular frequencies ω_{L_1} and ω_{L_2}. The longitudinal intensity profile of this superposition is shown in Fig. 1(a) for the case of $m = 14$. For a mode with a radial index $p = 0$, we see that the optical field [22] can be described by

$$
\begin{aligned}
\mathbf{E}(\mathbf{r}, t) = {} & \frac{\hat{\epsilon}\mathcal{E}_1 w_{0_1}}{2w_1(z)} \sqrt{\frac{1}{|m|!}} \left[\frac{\sqrt{2}\rho}{w_1(z)} \right]^{|m|} L_0^{|m|} \left[\frac{2\rho^2}{w_1(z)^2} \right] \exp\left[\frac{-\rho^2}{w_1(z)^2} \right] \exp\left[\frac{-ik_1\rho^2}{2R_1(z)} \right] \exp[i\psi_1(z)] \exp\left[i(m\phi - k_1 z) + i\omega_{L_1} t \right] \\
& + \frac{\hat{\epsilon}\mathcal{E}_2 w_{0_2}}{2w_2(z)} \sqrt{\frac{1}{|m|!}} \left[\frac{\sqrt{2}\rho}{w_2(z)} \right]^{|m|} L_0^{|m|} \left[\frac{2\rho^2}{w_2(z)^2} \right] \exp\left[\frac{-\rho^2}{w_2(z)^2} \right] \exp\left[\frac{-ik_2\rho^2}{2R_2(z)} \right] \exp[i\psi_2(z)] \\
& \times \exp\left[-i(k_2 z + m\phi) + i\omega_{L_2} t \right] + \text{c.c.},
\end{aligned}
\tag{1}
$$

where

$$
w_i(z) = w_{0_i}\sqrt{1 + (z/z_{R_i})^2},
\tag{2}
$$

$$
R_i(z) = z + \frac{z_{R_i}^2}{z},
\tag{3}
$$

$$
\psi_i(z) = (|m| + 1) \arctan(z/z_{R_i}),
\tag{4}
$$

and $\mathbf{r} = (x, y, z) = (\rho, \phi, z)$ is a position vector in the laboratory frame. The vector $\mathbf{r}$ is the vectorial sum of the atom's center-of-mass position $\mathbf{R}$ and the relative coordinate $\mathbf{r}_e$ of the Rydberg electron. We assume that the beam has a linear polarization described by the unit vector $\hat{\epsilon}$. The parameters z_{R_i} and w_{0_i} are the Rayleigh ranges and waists of the beams, respectively, for $i = 1$ and 2. Note that we use the convention $\mathcal{E}_i = \sqrt{\frac{2I_i}{c\epsilon_0}}$ and $I_i = \frac{2P_{0_i}}{\pi w_{0_i}^2}$ with a power P_{0_i} and a peak intensity

I_i for mode i. As the energy splittings from a low-m_l Rydberg state to a CS Rydberg level range from the order of $h \times$ GHz to $h\times$ THz, the wavelengths of the two modes need only differ by a few nm or less. Thus, it is reasonable to focus the copropagating beams with the same optics and assume similar Rayleigh ranges.

Electromagnetic fields can be introduced in the minimal coupling Hamiltonian by including the vector potential $\mathbf{A}(\mathbf{r}, t)$ and scalar potential $\Phi(\mathbf{r})$. For $\Phi = 0$, noting that $\mathbf{E} = -\partial_t \mathbf{A}$ and using the harmonic nature of the assumed fields, we can include the vector potential $\mathbf{A}$ operator in the Hamiltonian H.

After including the harmonic vector potential, we see that the minimal coupling Hamiltonian becomes

$$H = \frac{1}{2m_e}(\mathbf{p} + e\mathbf{A})^2. \qquad (5)$$

The term proportional to A^2 consists of a time-dependent potential $V_C(\mathbf{r}, t)$ coupling a low-angular momentum Rydberg level to the CS and a time-independent electron trapping potential $V_p(\mathbf{r})$. Both of these potentials seen by a Rydberg electron on the xy plane are shown in Figs. 1(b) and 1(c). A scattering interaction between the two LG photons with opposite m is responsible for the time-dependent part of the ponderomotive potential. This is given by

$$V_C(\mathbf{r}, t) = 4^{|m|} \frac{(2|m|)!}{|m|!} \sqrt{\frac{4\pi}{(4|m| + 1)!}} \left(\frac{e^2 \sqrt{I_1 I_2} w_{0_1} w_{0_2}}{m_e c \epsilon_0 \omega_{L_1} \omega_{L_2}} \right)$$
$$\times r^{2|m|} [w_1(r \cos\theta) w_2(r \cos\theta)]^{-(|m|+1)}$$
$$\times \exp(-r^2 \sin^2\theta [w_1(r \cos\theta)^{-2} + w_2(r \cos\theta)^{-2}])$$
$$\times \left[Y_{2|m|}^{2m}(\theta, \phi) S(\mathbf{r}) \exp(-i\omega_b t) \right.$$
$$\left. + Y_{2|m|}^{-2m}(\theta, \phi) S^*(\mathbf{r}) \exp(i\omega_b t) \right], \qquad (6)$$

with a phase term

$$S(\mathbf{r}) = \exp\left[\frac{ir^2 \sin^2\theta}{2} \left(\frac{k_2}{R_2(r \cos\theta)} - \frac{k_1}{R_1(r \cos\theta)} \right) \right]$$
$$\times \exp\{i[\psi_1(r \cos\theta) - \psi_2(r \cos\theta)]\}$$
$$\times \exp[i(k_2 - k_1)r \cos\theta], \qquad (7)$$

where $\omega_b = \omega_{L_2} - \omega_{L_1}$. From Eq. (6), it is seen that the time-dependent potential V_C drives transitions between Rydberg-state pairs with energy difference $\hbar\omega_b$. The spatial structure of V_C, visualized in Fig. 1(c), determines the coupling matrix element between them. For the conditions discussed in this paper, $S(\mathbf{r})$ is virtually identical to unity; therefore, we set $S(\mathbf{r}) = 1$.

The static electron trapping potential V_p is given by

$$V_p(\mathbf{r}) = \frac{e^2 I_1 w_{0_1}^2}{2|m|! m_e c \epsilon_0 \omega_{L_1}^2 [w_1(r \cos\theta)]^2} \left[\frac{2r^2 \sin^2\theta}{w_1(r \cos\theta)^2} \right]^{|m|}$$
$$\times \exp\left[\frac{-2r^2 \sin^2\theta}{w_1(r \cos\theta)^2} \right] + \frac{e^2 I_2 w_{0_2}^2}{2|m|! m_e c \epsilon_0 \omega_{L_2}^2 [w_2(r \cos\theta)]^2}$$
$$\times \left[\frac{2r^2 \sin^2\theta}{w_2(r \cos\theta)^2} \right]^{|m|} \exp\left[\frac{-2r^2 \sin^2\theta}{w_2(r \cos\theta)^2} \right]. \qquad (8)$$

The trapping potential V_p, visualized in Fig. 1(b), acts on the quasifree Rydberg electron and radially traps the atoms within
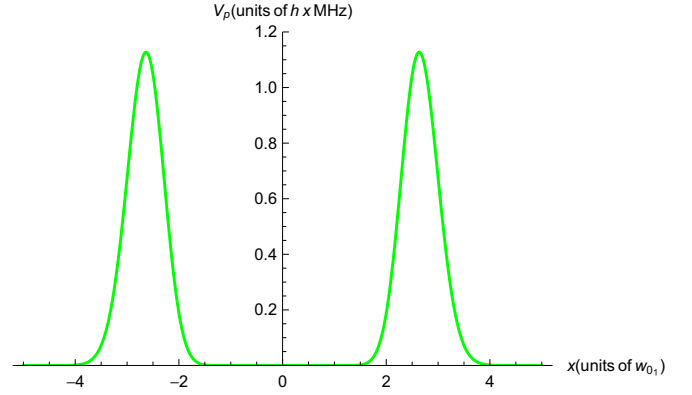

FIG. 2. Ponderomotive electron trapping potential included in the Hamiltonian as seen along the x axis of the laboratory frame for $\lambda_1 = 536$ nm and $\lambda_2 = 532$ nm, where the origin is placed at the center of the LG modes of $m = 14$ with $w_{0_1} = 3.41$ μm and $w_{0_2} = 3.39$ μm. This potential is plotted for total powers $P_{0_1} = P_{0_2} = 150.0$ mW.

the center of the modes, for the intensity scales as ρ^{2m} as $\rho \to 0$. In Fig. 2, we plot a cut through V_p for laser modes with wavelengths $\lambda_1 = 536$ nm and $\lambda_2 = 532$ nm.

When making the rotating-wave approximation, we neglected several terms in the A^2 part of the Hamiltonian that are highly energy nonconserving on optical energy scales; these terms correspond the absorption of photon pairs or emission of photon pairs.

B. Rabi frequency

An S-state Rydberg atom's radius scales as $2n^2 a_0$. However, as the angular momentum of a Rydberg atom increases, its radius decreases. For a CS, the radius is $n^2 a_0$. Therefore, it is not feasible to circularize Rydberg atoms of the same n in a single step due to small wave function overlap. For optimal Rabi frequencies, one must choose a CS of a principal quantum number n' and a low-m_l Rydberg atom of principal quantum number $n \simeq n'/\sqrt{2}$. For this calculation, we choose to transfer $|g\rangle = |21\mathrm{F}_{7/2}, m_l = 3\rangle$ atoms to $|e\rangle = |n = 32, l = 31, m_l = 31\rangle$. The overlap of the radial wave functions $U_g(r_e), U_e(r_e)$ of these two states is exhibited in Fig. 3.

The energy splitting between $|g\rangle$ and $|e\rangle$ is $h \times 4.2$ THz. That means we must choose LG modes with frequencies such that $\omega_b = 2\pi \times 4.2$ THz. We choose to model an experiment in which λ_1, the wavelength of LG mode 1 is 536 nm, and $\lambda_2 = 532$ nm, which are both far off-resonant from any transition in ^{85}Rb, the alkali we use. These copropagating LG modes give rise to a ponderomotive interaction term $V_C(\mathbf{r}, t)$ in the Hamiltonian [see Eq. (6)]. To calculate the Rabi frequency for this transition as a function of atomic center-of-mass position $\mathbf{R}$, we must obtain matrix element $\langle e|V_C(\mathbf{R} + \mathbf{r}_e)|g\rangle$ by integrating over the relative Rydberg-electron coordinate $\mathbf{r}_e$. Thus, we calculate the Rabi frequency

$$\Omega(\mathbf{R}) = \frac{2}{\hbar} \int \psi_e^*(\mathbf{r}_e) V_C(\mathbf{R} + \mathbf{r}_e) \psi_g(\mathbf{r}_e) d^3 r_e, \qquad (9)$$
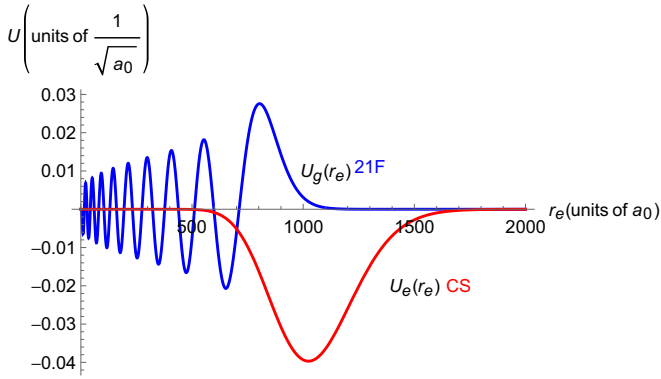
FIG. 3. Radial wave function overlap of the states discussed in the text: $|g\rangle$ (blue) and $|e\rangle$ (red).

where $\psi_g(\mathbf{r}_e)$ and $\psi_e(\mathbf{r}_e)$ are the electronic wave functions of $|g\rangle$ and $|e\rangle$, respectively. Due to negligible quantum defects for both states, the radial wave functions can be assumed to be hydrogenic. For our calculations, we use the parameters of optical power $P_{0_1} = P_{0_2} = 150$ mW and waists $w_{0_1} = 3.41 \ \mu$m and $w_{0_2} = 3.39 \ \mu$m. The Rabi frequencies presented in Fig. 4 are numerically integrated with a quasi-Monte Carlo algorithm.

C. Adiabatic potentials

In general, states $|g\rangle$ and $|e\rangle$ will see different ponderomotive energy shifts introduced by $V_p(\mathbf{R} + \mathbf{r}_e)$. These energy shifts are on the order of the Rabi frequency and are responsible for a cylindrical trap for the Rydberg atoms. Through the application of external magnetic and electric fields, it can be ensured that the perturbations of the ponderomotive potential are much less than the external-field-induced frequency splittings among the relevant atomic states. Thus, we can assume that the electron's wave function is the same for all center-of-mass positions $\mathbf{R}$. To determine the ponderomotive energy shift as a function of center-of-mass position for the CS, we calculate the Born-Oppenheimer adiabatic potential
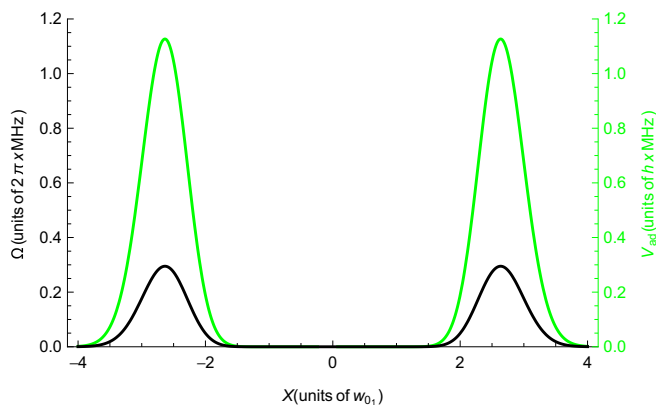

FIG. 4. Adiabatic potential (green) seen by the CS atom of $n = 32$ as a function of the atom's center-of-mass position along the X axis for $w_{0_1} = 3.41 \ \mu$m $w_{0_2} = 3.39 \ \mu$m and $P_{0_1} = P_{0_2} = 150$ mW. The Rabi frequency (black) for the transition of 21F to the CS of $n = 32$ along the X axis for the same optical parameters.

from nondegenerate perturbation theory:

$$V_{\mathrm{ad}}(\mathbf{R}) = \int \psi_e^*(\mathbf{r}_e) V_p(\mathbf{R} + \mathbf{r}_e) \psi_e(\mathbf{r}_e) d^3 r_e. \tag{10}$$

Numerical integration of Eq. (10) with a quasi-Monte Carlo algorithm results in the energy shifts shown in Fig. 4 for $|e\rangle$ along the X axis. Because the diameters of the atoms in states $|g\rangle$ and $|e\rangle$ are $\sim$90 nm and the diameter of the radial trap is $\sim$20 μm, these low-n Rydberg atoms are effectively pointlike particles with respect to the trap's intensity profile. Therefore, through calculation of Eq. (10), there is little spatial averaging over the electron's wave function and $V_{\mathrm{ad}} \simeq V_p$ in magnitude. As a result, $|g\rangle$ and $|e\rangle$ see the same adiabatic potential.

D. Experimental considerations

The difference in level shifts ΔV_{ad}, i.e., the adiabatic potential of $|g\rangle$ subtracted from that of $|e\rangle$, has a dependence on $\mathbf{R}(t)$, the center-of-mass position as a function of time. However, as mentioned above, because the wave functions of $|g\rangle$ and $|e\rangle$ have similar sizes, the trap is nearly magic, as it has a maximum ΔV_{ad} of 0.7 kHz. To evaluate the circularization efficiency, it is required to consider the trajectories of the trapped atoms. We can extract $\mathbf{R}(t)$ from Newton's equations by treating the atoms as classical bodies in a two-dimensional trapping potential. The trapped atoms can be modeled by an ensemble with a uniform spatial distribution and a Maxwell-Boltzmann distribution of speed. A typical rms speed of an atom in a Rb corkscrew molasses is $v_0 = 5$ cm/s. Simulations show that this case would lead to a typical round-trip period of 0.6 ms for the aforementioned parameters. Given that the lifetime of a ^{85}Rb Rydberg atom in the 21F state is $\tau_{21F} = 11 \ \mu$s, the period is almost 60 times the lifetime of an atom in the 21F state in a 300 K blackbody field, meaning that the atoms excited into the 21F state with an initial center-of-mass position at the center of the trap would decay before they reach the trap walls (where they would become circularized if they were still in 21F). Therefore, only the atoms initially close to the edge of the trap have a chance of becoming circularized. For an atom to become circularized, it has to be laser-excited into 21F sufficiently close to a peak in Fig. 4 so it can reach the trapping-light field within the 21F radiative decay time, τ_{21F}. The maximum distance is $dr \sim v_0 \tau_{21F}$. The cross-sectional area of the ring corresponding to the set of points that are within a distance dr from the circle that outlines the intensity maximum of the cylindrically symmetric trap beam is about $2\pi r_0 dr$, with $r_0 \approx 10 \ \mu$m denoting the radius of the trap (see Fig. 4). With the total cross-sectional area of the trap, πr_0^2, the fraction of 21F atoms that can reach the circularization area is seen to be $\sim 2 v_0 \tau_{21F}/r_0$. Further, since the Rabi frequency for optical circularization is several 100 kHz (see Fig. 4), the circularization probability for 21F atoms within the trap-beam light field is about 50%. It is concluded that the circularization probability for all 21F atoms generated is $\sim$5%.

The energy splitting between $|g\rangle$ and $|e\rangle$ is several THz to guarantee sufficient wave function overlap. It is not trivial to phase lock two lasers with a THz frequency difference. A possible realization of this scheme is the following. Two tunable lasers at 532 nm (beam 1) and 536 nm (beam 2) are phase locked to two modes of a frequency comb laser separated by

4.2 THz and diffract off spatial light modulators (SLMs) or digital micromirror devices (DMDs) to give opposite winding numbers 14 and -14 [23]. When the beams are combined, they overlap a cold sample of ^{85}Rb, prepared in an optical molasses at $\sim 10\ \mu$K. Cold atoms are adiabatically loaded into the radial trap by slowly ramping up beam 1 to allow efficient cooling within the center of the LG beams, while keeping beam 2 off. The highly blue-detuned frequencies of the LG modes provide a repulsive dipole force on ground-state ^{85}Rb atoms, confining them inside the cylindrical region formed by the beams. The atoms are then optically pumped into the $|5S_{1/2}, m_F = 3\rangle$ Zeeman sublevel with a 780-nm laser of σ^+-polarization. Subsequently, the sample is excited to $|g\rangle$ with 780-nm, 776-nm, and 1292-nm lasers of σ^+-polarizations pulsed on for a duration of $\sim 1\ \mu$s. Beam 2 is then pulsed on for a duration on the order of τ_{21F}. The timing and pulse shapes of this procedure may be optimized by quantum optimal control theory to yield the highest fidelity [12,13].

III. RAPID ADIABATIC PASSAGE IN AN RF-MODULATED PONDEROMOTIVE OPTICAL LATTICE

In the previous section, we considered a case where an atom is circularized by a single ponderomotive interaction that is highly forbidden for an electric-dipole interaction ($\Delta m_l = 28$). For this section, we consider many quadrupole-like ponderomotive interactions that lead to circularization in a RAP scheme [10,11]. We consider an optical lattice that is a superposition of a laser beam shifted in frequency by $\omega_{\rm rf}$ and an unmodulated beam. We can use the effects of the ponderomotive interaction [19,20] to couple states for the RAP method. For this calculation, we consider the hydrogenic states of the $n = 32$ Rydberg level under static, homogeneous fields $F = 2.736$ V/cm and $B = 5.0$ G. Also, we assume the carrier frequency of the laser is 532 nm. The bound-state energy W, in the parabolic basis of $|n, n_1, n_2, m_l\rangle$, with $n = n_1 + n_2 + |m_l| + 1$, is given by

$$W = -hc\left(\frac{m_+}{m_e + m_+}\right)\frac{R_\infty}{n^2} + \frac{3}{2}Fea_0n(n_1 - n_2)$$
$$+ \frac{e\hbar B}{2m_e}(m_l + g_s m_s) - \frac{1}{4}\pi\epsilon_0 a_0^3 F^2 n^4$$
$$\times \left[17n^2 - 3(n_1 - n_2)^2 - 9m_l^2 + 19\right], \quad (11)$$

where m_+ is the mass of the ^{85}Rb ion core, R_∞ is the Rydberg constant, $g_s = 2$, and m_s is the Zeeman sublevel of the electron's spin. The last term of W is responsible for modeling the energy splittings in the quadratic Stark effect.

While the static fields are polarized along the quantization-axis $\hat{z}$, the POL propagates along $\hat{x}$ and is polarized along $\hat{y}$. It is important to note that because the theory of RAP is best-described in the dressed-atom picture, we represent the POL laser's vector potential as

$$\mathbf{A}(\mathbf{r}, t) = \hat{y}\sum_{\mathbf{k}}\frac{\mathcal{E}_{\mathbf{k}}}{2\omega_{\mathbf{k}}}a_{\mathbf{k}}e^{i(\mathbf{k}\cdot\mathbf{r}-\omega_{\mathbf{k}}t)} + {\rm H.c.}, \quad (12)$$

with $\mathcal{E}_{\mathbf{k}}$ being the quantized field amplitude ($\sqrt{\frac{2\hbar\omega_{\mathbf{k}}}{\epsilon_0\mathcal{V}}}$) and $a_{\mathbf{k}}$ being the annihilation operator for mode $\mathbf{k}$. Recall that $\mathbf{r}$ is the

position vector in the laboratory frame that is the sum of the atom's center-of-mass position $\mathbf{R}$ and the Rydberg electron's relative coordinate $\mathbf{r}_e$. For the case of a modulated POL, $\mathbf{k} = \pm\mathbf{k}_1, \pm\mathbf{k}_2$ with $\mathbf{k}_1$ being the wave vector corresponding to the unmodulated mode with angular frequency ω_L and $\mathbf{k}_2$ corresponding to the mode modulated by $\omega_{\rm rf}(t)$. The minus signs correspond to the backward-propagating modes. The angular frequency accompanying mode $\mathbf{k}$ is denoted by $\omega_{\mathbf{k}}$. If we consider the atom in the presence of parallel electric and magnetic fields, F and B, respectively, we can make the Born-Oppenheimer approximation by adiabatically separating $\mathbf{R}$, the center-of-mass position in the laboratory frame, from $\mathbf{r}_e$, the electron's position in the atom's frame. Under the assumptions of real field amplitudes and a perfectly balanced lattice, the quasi-free-electron ponderomotive term $\frac{e^2 A(\mathbf{r}=\mathbf{R}+\mathbf{r}_e,t)^2}{2m_e}$ gives an interaction potential $V_{\rm AF}(\mathbf{R} + \mathbf{r}_e, t)$ described by

$$V_{\rm AF}(\mathbf{R} + \mathbf{r}_e, t) = \frac{e^2 f(t)\mathcal{E}_{\mathbf{k}_2}\mathcal{E}_{\mathbf{k}_1}}{4m_e\omega_L[\omega_L + \omega_{\rm rf}(t)]}$$
$$\times \left\{a_{\mathbf{k}_2}a^\dagger_{-\mathbf{k}_1}\exp[i(k_1 + k_2)(X + x_e)]\right.$$
$$\left. + a_{-\mathbf{k}_2}a^\dagger_{\mathbf{k}_1}\exp[-i(k_1 + k_2)(X + x_e)]\right\}, \quad (13)$$

where $a_{\pm\mathbf{k}_2}$ and $a^\dagger_{\pm\mathbf{k}_1}$ are, respectively, the annihilation and creation operators for a modulated mode and an unmodulated mode. The modulated mode also has a temporal envelope described by $f(t)$. Because the rf frequency is so much smaller than the optical frequency of the lattice, we can neglect the $\omega_{\rm rf}(t)$ in the denominator of Eq. (13). Note that we adopt the rotating-wave approximation to arrive at Eq. (13).

The interaction modeled by Eq. (13) describes the inelastic scattering process of a forward-propagating modulated photon into an unoccupied backward-propagating mode. During the scattering process, the modulated photon imparts its rf energy to the atom, promoting it to a state with $\Delta m_l = 2$, as shown in Fig. 5.

The POL interacts with hydrogenic states of a principal quantum number n with Zeeman sublevels m_l and parabolic numbers $n_1 = 0$, and $n_2 = n - 1 - m_l$. Additionally, because we work in the dressed-atom picture involving photons of modes $\pm\mathbf{k}_2$ and $\mp\mathbf{k}_1$, we must include their photon numbers, which we will represent by $N + n_2/2$ and $M - n_2/2$, respectively, where N and M are background photon numbers that can be set to zero in the energy eigenvalues, as they contribute the same offset for each state. Note that if we assume a perfectly balanced lattice, there are the same number of photons for modes $\mathbf{k}$ and $-\mathbf{k}$. Thus, we characterize the dressed states with $|i\rangle = |m_l, n_2 = n - 1 - m_l, N + n_2/2, M - n_2/2\rangle$ and eigenvalues

$$W_i'(t) = W + \frac{n_2}{2}\hbar(\omega_{\rm rf} + \alpha t) + V_{{\rm ad},n_2,m_l}, \quad (14)$$

where $V_{{\rm ad},n_2,m_l}$ is the offset of the ponderomotive lattice shift, which is determined to differ among states within $n = 32$. The modulator imprints a phase of $-\frac{1}{2}(2\omega_{{\rm rf},0}t + \alpha t^2)$ on the transmitted wave for a POL that is chirped with a frequency
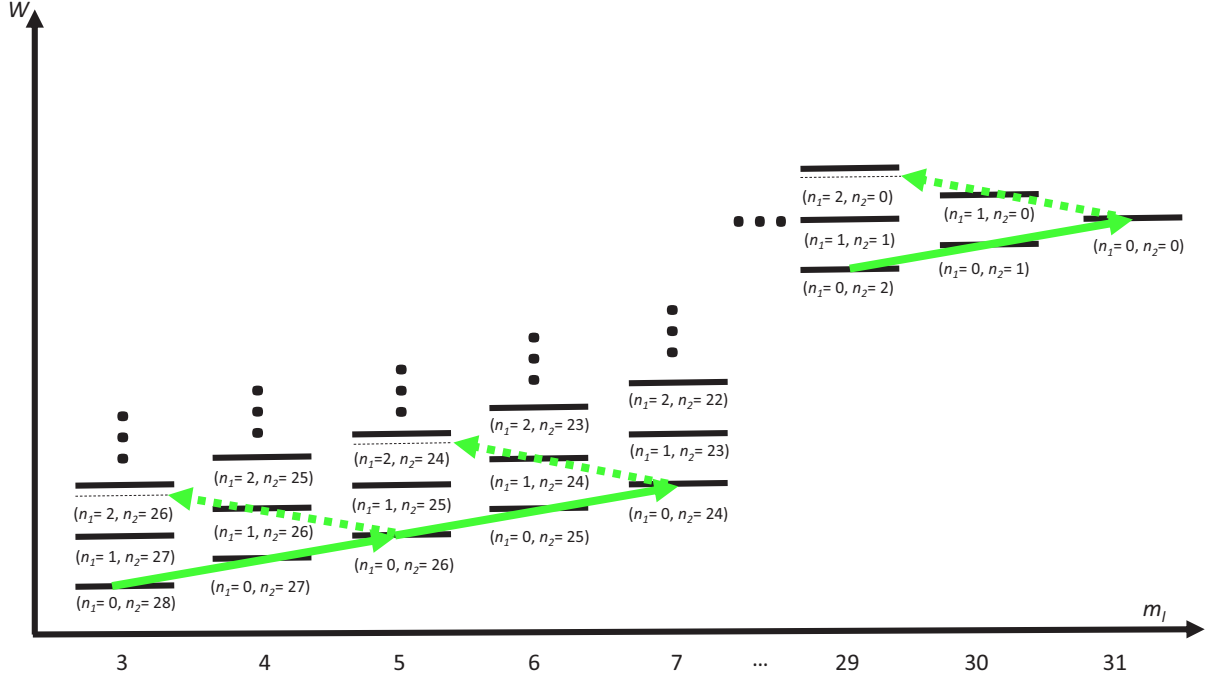
FIG. 5. Hydrogenic manifold in the parabolic basis $n = n_1 + n_2 + |m_l| + 1$ under parallel electric and magnetic fields F and B. The solid green arrows represent desired couplings provided by the rf-modulated POL; the dashed lines represent undesired "leakage" transitions that reduce the overall circularization efficiency. Magnetic field B detunes these "leakage" transitions from resonance and minimizes CS population loss from them.

range $\Delta \nu$ over a period τ, where $\alpha = 2\pi \frac{\Delta \nu}{\tau}$ [24] and $\omega_{\text{rf},0}$ is the rf center frequency.

The relevant eigenstates for $n = 32$ and $n_1 = 0$ are represented as coherent superpositions of spherical hydrogenic states given by

$$
\begin{aligned}
&|m_l, n_2, N + n_2/2, M - n_2/2\rangle \\
&= \sum_l (-1)^{(-31 + m_l - n_2)/2 + l} \sqrt{2l + 1} \\
&\times \begin{pmatrix} \frac{31}{2} & \frac{31}{2} & l \\ \frac{m_l - n_2}{2} & \frac{m_l + n_2}{2} & -m_l \end{pmatrix} |n = 32, l, m_l\rangle \\
&\otimes |N + n_2/2, M - n_2/2\rangle,
\end{aligned} \tag{15}
$$

where the terms in parentheses are the Wigner 3-j symbol [25].

In the limit of strong laser fields, the interaction potential becomes

$$
\begin{aligned}
V_{\text{AF}}(\mathbf{R} + \mathbf{r}_e, t) = \frac{e^2 e^{-\ln(16)t^2/2\tau^2} \sqrt{I_{\mathbf{k}_1} I_{\mathbf{k}_2}}}{m_e c \epsilon_0 \omega_L^2} \\
\times \cos[(k_1 + k_2)(X + x_e)].
\end{aligned} \tag{16}
$$

Also, we set $f(t) = e^{-\ln(16)t^2/2\tau^2}$. An atom sitting at the bottom of a potential well will see a quadratic potential approximated by

$$
\begin{aligned}
V_{\text{AF}}(\mathbf{r}_e) \simeq \frac{e^2 e^{-\ln(16)t^2/2\tau^2} \sqrt{I_{\mathbf{k}_1} I_{\mathbf{k}_2}} (k_1 + k_2)^2}{2 m_e c \epsilon_0 \omega_L^2} r_e^2 \\
\times \left[\sqrt{\frac{2\pi}{15}} Y_2^2(\theta_e, \phi_e) + \sqrt{\frac{2\pi}{15}} Y_2^{-2}(\theta_e, \phi_e) + \frac{\sin^2 \theta_e}{2} \right],
\end{aligned} \tag{17}
$$

which corresponds to a nondiagonal matrix element of

$$
\begin{aligned}
\langle m_l + 2, n_2 - 2 | V_{\text{AF}}(\mathbf{r}_e) | m_l, n_2 \rangle \simeq \frac{e^2 e^{-\ln(16)t^2/2\tau^2}}{4 m_e c \epsilon_0 \omega_L^2} \sqrt{2 I_{\mathbf{k}_1} I_{\mathbf{k}_2}/3} (k_1 + k_2)^2 \sum_{l, l'} (-1)^{-31 - n_2 + l + l'} (r_e^2)_l^{l'} \\
\times (2l + 1)(2l' + 1) \begin{pmatrix} \frac{31}{2} & \frac{31}{2} & l' \\ \frac{m_l - n_2}{2} + 2 & \frac{m_l + n_2}{2} & -m_l - 2 \end{pmatrix} \\
\times \begin{pmatrix} l & 2 & l' \\ m_l & 2 & -m_l - 2 \end{pmatrix} \begin{pmatrix} l & 2 & l' \\ 0 & 0 & 0 \end{pmatrix} \begin{pmatrix} \frac{31}{2} & \frac{31}{2} & l \\ \frac{m_l - n_2}{2} & \frac{m_l + n_2}{2} & -m_l \end{pmatrix},
\end{aligned} \tag{18}
$$

where $(r_e^2)_l^{l'}$ is the radial matrix element between two hydrogenic states in the spherical basis.

Nonadiabatic transitions that reduce the efficiency of RAP schemes are best modeled using the Schrödinger equation in

the adiabatic basis. The adiabatic eigenkets $|j\rangle$ of this Hamiltonian can be obtained by applying a unitary transformation [26,27] D, where

$$|j\rangle = \sum_i D_{ij}|i\rangle. \qquad (19)$$

Additionally,

$$|i\rangle = \sum_j D_{ji}^*|j\rangle. \qquad (20)$$

Thus, for quantum state $|i\rangle$ with Schrödinger equation

$$\sum_j [i\hbar\partial_t(D_{ji}^*|j\rangle) = HD_{ji}^*|j\rangle], \qquad (21)$$

$$\sum_j [i\hbar\dot{D}_{ji}^*|j\rangle + i\hbar D_{ji}^*\partial_t|j\rangle = \hat{H}D_{ji}^*|j\rangle], \qquad (22)$$

$$\sum_j [\langle j'|i\hbar D_{ij'}\dot{D}_{ji}^*|j\rangle + \langle j'|i\hbar D_{ij'}D_{ji}^*\partial_t|j\rangle$$
$$= \langle j'|D_{ij'}HD_{ji}^*\delta_{jj'}|j\rangle], \qquad (23)$$

where the $\langle j'|i\hbar D_{ij'}\dot{D}_{ji}^*|j\rangle$ term is responsible for nonadiabatic transitions from one adiabatic ket, $|j\rangle$, to another, $|j'\rangle$. The idea behind the RAP method is to minimize this term such that a state initialized at $m_l = 3$ arrives at $m_l = 31$ at the end of the frequency chirp. Efficiency of this process is diminished if atoms are lost to other adiabatic states via nonadiabatic transitions.

In the regime in which the Rabi frequency is lower than the splittings of the second-order Stark effects and ponderomotive shifts, the RAP involves sequential two-level Landau-Zener transitions into the CS. The probability of atoms in state $|j\rangle$ transitioning to $|j'\rangle$ is, as presented in Refs. [26,28],

$$P(j \to j') = e^{-2\pi\Gamma}, \qquad (24)$$

where

$$\Gamma = \frac{|\langle i'|V_{\mathrm{AF}}|i\rangle|^2}{\hbar|d[W_{i'}'(t) - W_i'(t)]/dt|}. \qquad (25)$$

To achieve a nonadiabatic transition probability lower than ~ 0.01, $2\pi\Gamma \gg 4$. However, we calculate Rabi frequencies as high as $2\pi \times 1.90\,\mathrm{MHz}$ for the case of a perfectly balanced lattice consisting of 1.43 W modulated and unmodulated beams focused to a waist of $10\,\mu\mathrm{m}$. These coupling strengths put us in a regime where the atom transitions into multiple states at a time, as shown in Fig. 6(a), making two-level Landau-Zener models inaccurate.

Figure 6(a) shows the population P of atoms occupying the lowest ladder of the hydrogenic manifold in parabolic coordinates for $\tau = 25\,\mu\mathrm{s}$ and $\Delta\nu = 1.41\,\mathrm{MHz}$ for a Gaussian amplitude modulation and a linear chirp. Notice that the beginning of the chirp rate seems to have the behavior of a two-level Landau-Zener transition. That is because there exists a differential ponderomotive shift ΔV_{ad} between atoms in $m_l = 3$ and those in $m_l = 5$ are comparable to the Rabi frequency of the coupling between them, i.e., $\Omega = 2\pi \times 1.04\,\mathrm{MHz}$ and $\Delta V_{\mathrm{ad}}/\hbar = 2\pi \times 1.28\,\mathrm{MHz}$ for atoms situated at the bottom of a lattice well. Throughout the middle of the RAP procedure, the Rabi frequencies are much larger and allow multiple nonadiabatic states to be excited at the same time. We find a
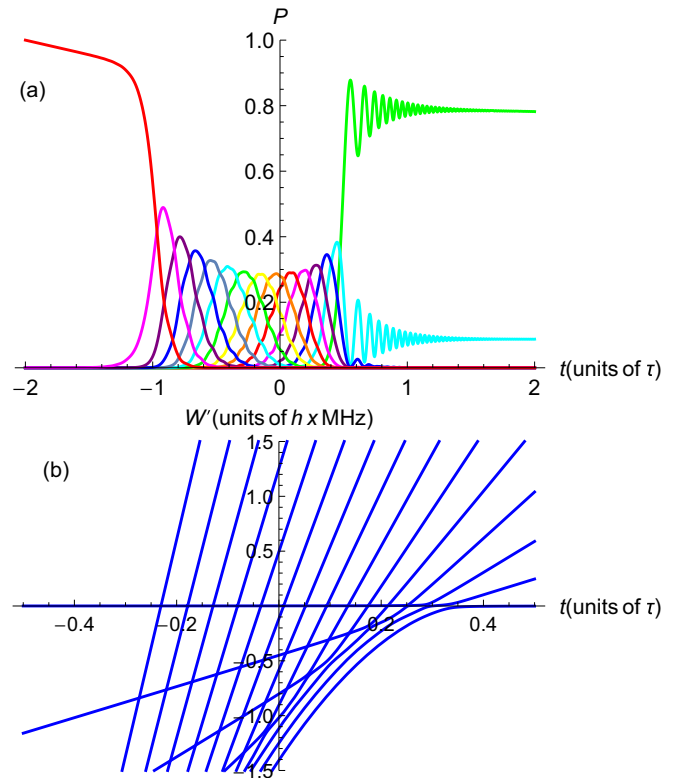

FIG. 6. In (a), we display the probability of atoms populating hydrogenic states from $|3, 28, N + 14, M - 14\rangle$ to the CS, $|31, 0, N, M\rangle$, as a function of time scaled by $\tau = 25\,\mu\mathrm{s}$ and $\Delta\nu = 1.41\,\mathrm{MHz}$. The rightmost green curve displays the probability of atoms populating the CS, while the leftmost red curve represents the population of atoms in the $|3, 28, N + 14, M - 14\rangle$ state. In (b), we show the adiabatic eigenenergies of the Hamiltonian dressed by the inelastic scattering interactions of the lattice photons.

circularization efficiency of nondecayed Rydberg atoms from this simulation to be 89%. Including Rydberg-atom decay in the simulation, the circularization efficiency drops to 77%.

While $n = 32$ Rydberg atoms with low angular momenta would decay from radiative losses after $\sim 50\,\mu\mathrm{s}$ in a 4 K environment, CS atoms shielded from thermal photons would live much longer, at the order of $\sim 10\,\mathrm{ms}$. The development of a nonlinear chirp that maintains an average rate equal to α, yet scans more quickly during the passage through low-m_l states than the rate through high-m_l states, would circumvent this issue.

The leakage transitions represented by the dashed lines in Fig. 5 can lead to a significant reduction of the atoms in the CS at the end of the sequence. Circularization schemes involving RAP with linearly polarized couplings require the application of a magnetic field to lift the degeneracy of the unwanted and desired transitions [10]. For our calculation, where these transitions differ in resonant frequency by $\sim 28\,\mathrm{MHz}$, we restrict the Hilbert space to states with $n_1 = 0$ and $m_l \geqslant 3$, as the magnetic-field-induced detuning of 28 MHz is assumed to be strong enough to inhibit the leakage transitions into other states.

The experimental realization of this method would require constructing a POL with a high-powered laser beam split in a

Mach-Zehnder interferometer with one arm acousto-optically modulated by an rf source of center angular frequency $\omega_{\mathrm{rf},0} = 2\pi \times 350\,\mathrm{MHz}$ and the other unmodified. Suitable electrode and Helmholtz coil geometries would allow the static fields used in this calculation.

IV. CIRCULARIZATION OF RYDBERG ATOMS IN A TIME-ORBITING PONDEROMOTIVE OPTICAL LATTICE

As previously mentioned, the fidelity of circularization schemes is reduced by unwanted transitions within the hydrogenic manifold if the polarization of the coupling is not purely σ^+ or σ^-. In this section, we will show that a TOPOL, with effective electro-optic control, would provide potentials that would drive transitions equivalent to those of purely $\sigma^{\pm}$-polarized rf radiation.

The idea of the TOPOL is that the two-dimensional optical lattice is constructed by a ponderomotive potential with a rapidly orbiting, time-dependent component, resulting in a static part that is approximately harmonic and a time-dependent part that is equivalent to rotating rf electric field. Such a potential is realized by a two-dimensional POL with the x and y components phase shifted with a cosine and sinelike time dependence, respectively. To drive transitions between two Rydberg states, the phase-modulation frequency must be equal to the resonant frequency of a Rydberg transition. It will be shown that the effect is an electric-dipole coupling between Rydberg states in a manner such that m_l can only increase or decrease by one unit but not both.

Consider the intersection of four optical fields described by

$$\mathbf{E}_1^{(+)}(x, t) = \hat{\epsilon}^{(1)} \mathcal{E}_1^{(+)} \cos\left[kx - \omega_L t + \beta_x \cos(\omega_{\mathrm{rf}} t)\right], \quad (26)$$

$$\mathbf{E}_2^{(+)}(y, t) = \hat{\epsilon}^{(2)} \mathcal{E}_2^{(+)} \cos\left[ky - \omega_L t + \beta_y \sin(\omega_{\mathrm{rf}} t)\right], \quad (27)$$

$$\mathbf{E}_1^{(-)}(x, t) = \hat{\epsilon}^{(1)} \mathcal{E}_1^{(-)} \cos(kx + \omega_L t), \quad (28)$$

$$\mathbf{E}_2^{(-)}(y, t) = \hat{\epsilon}^{(2)} \mathcal{E}_2^{(-)} \cos(ky + \omega_L t), \quad (29)$$

where $x = X + x_e$ and $y = Y + y_e$ are coordinates in the laboratory frame and β_x (β_y) is the amplitude of the phase shift of the beam forward propagating along $\hat{x}$ ($\hat{y}$). Here, we assume that $\beta_x = \beta_y = \beta$. We use the assumptions that the polarization vectors $\hat{\epsilon}^{(1)}$ and $\hat{\epsilon}^{(2)}$ are orthogonal and that the counterpropagating beams have polarizations parallel to those of the forward-propagating beams. Time integration of these fields yields the vector potential operators used in the minimal coupling Hamiltonian.

As a result, the electronic ponderomotive potential averaged over a phase-modulation cycle becomes

$$V_p(\mathbf{r}) = \frac{e^2}{c\epsilon_0 m_e \omega_L^2}\left[\sqrt{I_1^{(+)}I_1^{(-)}}J_0(\beta)\right.$$

$$\times \cos(2kx) + \sqrt{I_2^{(+)}I_2^{(-)}}J_0(\beta)\cos(2ky)$$

$$\left. + \frac{I_1^{(+)}J_0^2(\beta)}{2} + \frac{I_2^{(+)}J_0^2(\beta)}{2} + \frac{I_1^{(-)}}{2} + \frac{I_2^{(-)}}{2}\right], \quad (30)$$
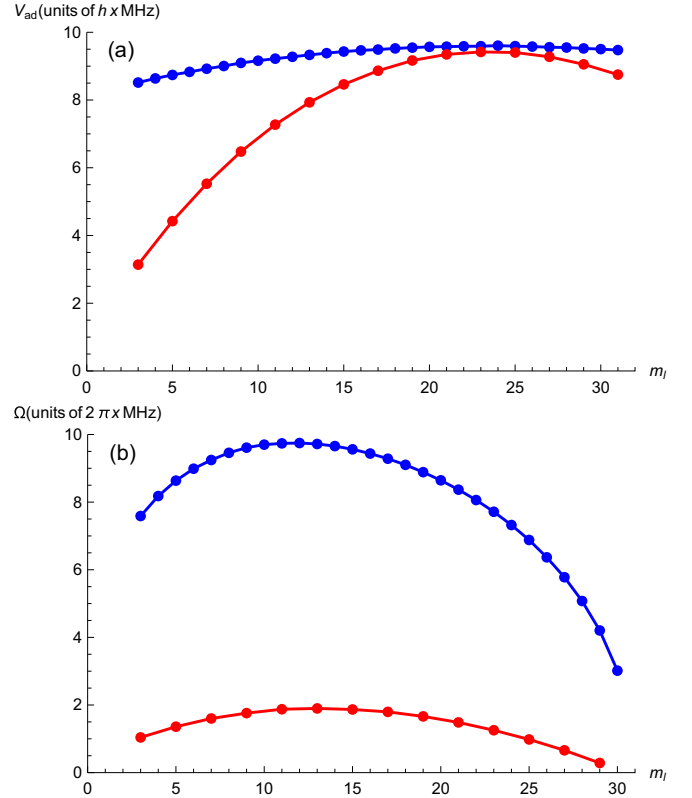

FIG. 7. (a) Ponderomotive shifts for an atom in state $|n = 32, n_1 = 0, n_2 = n - |m_l| - 1, m_l\rangle$ sitting at the bottom of a lattice well for the one-dimensional, rf-modulated POL described in the previous section (red) and for the TOPOL described in this section (blue). (b) Rabi frequencies coupling a state with m_l to $m_l + 2$ for the one-dimensional, rf-modulated POL (red) and with m_l to $m_l + 1$ for the TOPOL (blue).

where $I_i^{(+)}(I_i^{(-)})$ is the forward- (backward)-propagating peak intensity of lattice arm $i = 1, 2$. We ignore the higher-order phase-modulation terms. Numerically determined ponderomotive lattice shifts, V_{ad,n_2,m_l}, for atoms situated at the bottom of a well for each state $|m_l\rangle$ in the $n = 32$ hydrogenic manifold are shown in Fig. 7(a) and compared with the shifts in the previous section for the case of $I_1^{(+)} = I_2^{(+)} = I_1^{(-)} = I_2^{(-)} \simeq 0.907\,\mathrm{MW/cm}^2$ and $J_0(\beta) = 0.17$. We also set $k = 2\pi/532$ nm and assume sufficiently large stabilization fields F and B polarized along $\hat{z}$ to prevent state mixing.

The harmonic orbiting of the trap center at ω_{rf}, the resonant angular frequency for the transitions in the hydrogenic manifold, is modeled by the potential

$$V_{\mathrm{AF}}(x, y, t) = \frac{e^2}{c\epsilon_0 m_e \omega_L^2}\left\{\left[\sqrt{I_1^{(+)}I_1^{(-)}}J_1(\beta)\right.\right.$$

$$\times \sin(2kx) - i\sqrt{I_2^{(+)}I_2^{(-)}}J_1(\beta)\sin(2ky)\right]$$

$$\times e^{i\omega_{\mathrm{rf}}t} + \left[\sqrt{I_1^{(+)}I_1^{(-)}}J_1(\beta)\sin(2kx) + i\sqrt{I_2^{(+)}I_2^{(-)}}\right.$$

$$\left.\left.\times J_1(\beta)\sin(2ky)\right]e^{-i\omega_{\mathrm{rf}}t}\right\}. \quad (31)$$

Under the assumption that the atom's center-of-mass coincides with a lattice-well minimum and that the atom is small,

$$
\begin{aligned}
V_{\mathrm{AF}}(\mathbf{r}_e, t) \simeq \frac{\sqrt{8\pi/3}e^2 k r_e}{c\epsilon_0 m_e \omega_L^2} & \Big\{ \Big[\sqrt{I_1^{(+)} I_1^{(-)}} J_1(\beta_x) \\
& + \sqrt{I_2^{(+)} I_2^{(-)}} J_1(\beta) \Big] \big[Y_1^{-1}(\theta_e, \phi_e) e^{i\omega_{\mathrm{rf}}t} - Y_1^1(\theta_e, \phi_e) e^{-i\omega_{\mathrm{rf}}t} \big] \\
& + \Big[\sqrt{I_1^{(+)} I_1^{(-)}} J_1(\beta) - \sqrt{I_2^{(+)} I_2^{(-)}} J_1(\beta) \Big] \big[Y_1^{-1}(\theta_e, \phi_e) e^{i\omega_{\mathrm{rf}}t} \\
& - Y_1^1(\theta_e, \phi_e) e^{-i\omega_{\mathrm{rf}}t} \big] \Big\}.
\end{aligned}
\tag{32}
$$

If $\sqrt{I_1^{(+)} I_1^{(-)}} = \sqrt{I_2^{(+)} I_2^{(-)}}$, transitions from an unwanted helicity into lower-$|m_l|$ states cannot be driven. How well this condition is met determines how well the effective rf field is circularly polarized. After making the rotating-wave approximation and assuming that $\sqrt{I_1^{(+)} I_1^{(-)}} = \sqrt{I_2^{(+)} I_2^{(-)}} = \sqrt{I^{(+)} I^{(-)}}$, we arrive at an approximate dressed-atom Rabi frequency from Eq. (32), coupling states $|n, n_1 = 0; m_l, n_2\rangle$ and $|n, n_1 = 0; m_l + 1, n_2 - 1\rangle$, of

$$
\begin{aligned}
\Omega_{m_l, m_l+1} \simeq & \frac{4\sqrt{2}e^2 \sqrt{I^{(+)} I^{(-)}} J_1(\beta) k}{\hbar c\epsilon_0 m_e \omega_L^2} \sum_{ll'} (-1)^{-n-n_2+l'+l} (r_e)_l^{l'} (2l+1)(2l'+1) \\
& \times \begin{pmatrix} \frac{n-1}{2} & \frac{n-1}{2} & l \\ \frac{m_l-n_2}{2} & \frac{m_l+n_2}{2} & -m_l \end{pmatrix} \begin{pmatrix} l & 1 & l' \\ m_l & 1 & -m_l-1 \end{pmatrix} \begin{pmatrix} l & 1 & l' \\ 0 & 0 & 0 \end{pmatrix} \begin{pmatrix} \frac{n-1}{2} & \frac{n-1}{2} & l' \\ \frac{m_l-n_2}{2}+1 & \frac{m_l+n_2}{2} & -m_l \end{pmatrix}.
\end{aligned}
\tag{33}
$$

We numerically calculate these Rabi frequencies and plot them in Fig. 7(b) for the case of $I^{(+)} = I^{(-)} \simeq 0.907\,\mathrm{MW/cm^2}$ and $J_1(\beta) = 0.57$. For comparison, we also display the Rabi frequencies of the one-dimensional optical lattice described in the previous section.

In addition to the advantage of preventing leakage transitions, the TOPOL clearly provides stronger couplings. This is mainly because the ponderomotive term of the Hamiltonian provides a dipolelike potential which is proportional to a factor of k instead of k^2 as for the previously discussed lattice that provides quadrupolelike couplings for atoms at the center of the well. Also, notice that the variation in ponderomotive lattice shifts is lower for the TOPOL because the phase modulation reduces the trap depth by setting $J_0(\beta) = 0.17$. For a RAP scheme, this would allow more efficient transfer because all dressed states involved would meet closer to degeneracy when the modulation frequency is chirped. By using quantum optimal control theory by varying the TOPOL parameters, one could engineer pulses of $\beta_x \cos(\omega_{\mathrm{rf}}t)$ and $\beta_y \sin(\omega_{\mathrm{rf}}t)$ to obtain fast transfer to the CS on the order of $\sim$ ns and observe coherent Rabi oscillations between the F state and the CS [12,13].

V. DISCUSSION

We now give a discussion comparing each of our three proposed methods with each other and with the traditional methods of circularization that require quasistatic electromagnetic fields and free-space rf radiation. Among the traditional methods of circularization, the RAP method can be separated into two regimes based on the rf-induced coupling strength between atomic states. The method of RAP into the CS with weak rf couplings, initially performed in Ref. [9], consists of a series of sequential transitions of $\Delta m_l = 1$. A highly pure ensemble of CSs at the end of the RAP method is the main benefit of this scheme, in addition to the ease of only requiring linearly polarized rf radiation. However, RAP in the weak-field regime suffers from the extended duration of the process due to the need to meet the adiabaticity condition for each

consecutive transition [see Eq. (24)]. Another drawback is that this scheme limits the principal quantum number of the CS to $\sim$60. Additionally, the long ramping time of the dressed-state eigenenergies in this scheme limits the coherence time of the CS in applications that require a superposition of CSs and other hydrogenic states [29]. For the strong-field regime of RAP, where multiple hydrogenic states are excited at once, the procedure does not require as long ramping times and can be used in conjunction with quantum optimal control theory [12,13] to minimize the time of passage by means of pulse engineering. The disadvantage of this strong-field regime is that it often requires purely σ^+- or σ^--polarized rf radiation [11,12], or a sufficiently large magnetic field parallel to the electrostatic field [10] to prevent leakage transitions.

Advantages of the crossed-fields method include the versatility of circularizing within manifolds of higher principal quantum numbers. Also, there is no need for rf radiation at the location of the Rydberg atoms. As mentioned earlier, the crossed-fields method is susceptible to mixing of the CS with low-$|m_l|$ states by means of residual electric fields. The crossed-fields method is also not suitable for applications that require a quantization axis defined by the electrostatic field [2,11], as in such applications, one would have to suddenly turn on an electric field that is exactly parallel to the magnetic field. This effects a nonadiabatic transition of the CSs through a multilevel crossing that takes the atoms from the magnetically stabilized to the electrically stabilized regime. If there is any remaining perpendicular component of the electric field, the CS becomes contaminated in this process by reduction of $|m_l|$.

For preparation of an ensemble of cold CSs, laser cooling, trapping, and circularizaiton can all be done with laser fields at appropriate frequencies using the methods proposed in this paper based on an additional term in the minimal coupling Hamiltonian. In place of constructing in-vacuum and external electrodes and magnetic coils for the static and rf fields of the traditional methods, there is the technical convenience of aligning laser beams external to the vacuum chamber. We propose three schemes in this paper to cover a versatile range

of experimental contexts from high-precision spectroscopy to long-range interactions of Rydberg atoms. The method of circularization using LG beams would prepare a dilute, macroscopic sample of CSs that would increase the signal-to-noise ratio in spectroscopic experiments on CSs yet reduce density-dependent line broadening due to the low density of CS atoms produced in this method. Furthermore, because this method affords a single, direct coupling of the F state to the CS, the rate of circularization is faster than in low-field RAP methods, allowing the preparation of CSs to be done in low-intensity laser fields and weak, static stabilization fields, F and B, that are parallel. These weak fields provide smaller perturbations to the Rydberg ensemble, which benefits experiments in high-precision spectroscopy. Circularization via LG laser modes faces the experimental challenge of stabilizing a beat frequency at the order of a few THz and yields a low circularization efficiency of ~5%.

The one-dimensional, rf-modulated POL presented in Sec. III yields an appealing efficiency of 89%, is experimentally simple to construct with an acousto-optic modulator, and provides the control of Rydberg-Rydberg collisions with lattice depths. Additionally, this scheme could be useful for the study of magnetic phase transitions in a one-dimensional chain of Rydberg states [3]. Strong-coupling RAP using this scheme requires the application of a large magnetic field in order to prevent leakage transitions that could be experimentally difficult to switch because of eddy currents; this method also faces the issue of m_l-dependent ponderomotive shifts that need to be controlled, as exhibited in Fig. 7(a).

A superior method to the one-dimensional rf-modulated POL is the TOPOL presented in Sec. IV that does not require a large magnetic field for strong ponderomotive couplings due to the prevention of leakage transitions. With the TOPOL, a two-dimensional sample of CSs can be prepared with a spatial selectivity at the diffraction limit of the lattice beams. Furthermore, the TOPOL provides stronger couplings than the one-dimensional POL, as exhibited in Fig. 7(b), because the time-dependent ponderomotive potential effects an electric-dipole-like coupling of a circularly polarized rf field. One can also implement quantum optimal control theory for this configuration in order to select pulses for the rf modulation of the lattice that transfer the F-states to the CS in the shortest amount of time. This fast transfer minimizes decoherence due to stray electric and magnetic fields and would allow

realization of applications in quantum sensing and simulations of two-dimensional Ising models [29–31]. However, for the TOPOL, failure in matching the intensities and phases of the modulating rf and optical beams in each lattice arm, as well as the polarizations of forward and backward-propagating lattice beams will result in an effective elliptically polarized rf field from the ponderomotive coupling that would yield a low circularization fidelity. Thus, careful optical alignment is required for the TOPOL.

A key difference between our all-optical methods and the traditional circularization schemes is the requirement of trapping the atoms with optical fields to realize the ponderomotive atom-field couplings in the Hamiltonian. We therefore deem our methods not suitable for experiments with hot atomic beams because the atoms must be slow enough to be captured in the optical traps.

VI. CONCLUSION

In summary, we have proposed and discussed three experimental schemes for optical circularization of Rydberg atoms using ponderomotive laser traps. These theoretical investigations demonstrate the versatility of the emerging subfield of ponderomotive interactions with Rydberg atoms. Our proposals could address the difficulty of initializing a quantum system of CSs by using optical couplings instead of static and rf fields. It would be interesting to investigate multilevel Rydberg systems involving the direct optical coupling of a direct, first-order optical coupling of an F state with a CS [32], afforded by the method we proposed in Sec. II. Additionally, the TOPOL discussed in Sec. IV would allow a convenient means of initializing a long-lived, two-dimensional Ising model simulator [30,31]. Another proposed quantum simulator that would benefit from these three discussed methods would investigate the angular momentum transport of flexible Rydberg aggregates [33]. Furthermore, all three of these methods would advance the field of engineering Rydberg wave packets [34].

[1] S. Haroche, Rev. Mod. Phys. **85**, 1083 (2013).

[2] A. Ramos, K. Moore, and G. Raithel, Phys. Rev. A **96**, 032513 (2017).

[3] T. L. Nguyen, J.-M. Raimond, C. Sayrin, R. Cortinas, T. Cantat-Moltrecht, F. Assemat, I. Dotsenko, S. Gleyzes, S. Haroche, G. Roux *et al.*, Phys. Rev. X **8**, 011032 (2018).

[4] R. Pohl, A. Antognini, F. Nez, F. D. Amaro, F. Biraben, J. M. Cardoso, D. S. Covita, A. Dax, S. Dhawan, L. M. Fernandes *et al.*, Nature **466**, 213 (2010).

[5] D. Delande and J. C. Gay, Europhys. Lett. **5**, 303 (1988).

[6] J. Hare, M. Gross, and P. Goy, Phys. Rev. Lett. **61**, 1938 (1988).

[7] D. A. Anderson, A. Schwarzkopf, R. E. Sapiro, and G. Raithel, Phys. Rev. A **88**, 031401(R) (2013).

[8] A. A. Morgan, V. Zhelyazkova, and S. D. Hogan, Phys. Rev. A **98**, 043416 (2018).

[9] R. G. Hulet and D. Kleppner, Phys. Rev. Lett. **51**, 1430 (1983).

[10] P. Nussenzveig, F. Bernardot, M. Brune, J. Hare, J. M. Raimond, S. Haroche, and W. Gawlik, Phys. Rev. A **48**, 3991 (1993).

[11] R. Lutwak, J. Holley, P. P. Chang, S. Paine, D. Kleppner, and T. Ducas, Phys. Rev. A **56**, 1443 (1997).

[12] A. Signoles, E. K. Dietsche, A. Facon, D. Grosso, S. Haroche, J. M. Raimond, M. Brune, and S. Gleyzes, Phys. Rev. Lett. **118**, 253603 (2017).

[13] S. Patsch, D. M. Reich, J.-M. Raimond, M. Brune, S. Gleyzes, and C. P. Koch, Phys. Rev. A **97**, 053418 (2018).

[14] P. H. Bucksbaum, D. W. Schumacher, and M. Bashkansky, Phys. Rev. Lett. **61**, 1182 (1988).

[15] D. L. Freimund, K. Alfatooni, and H. Batelaan, Nature **413**, 142 (2001).

[16] S. K. Dutta, J. R. Guest, D. Feldbaum, A. Walz-Flannigan, and G. Raithel, Phys. Rev. Lett. **85**, 5551 (2000).

[17] K. Mukherjee, S. Majumder, P. K. Mondal, and B. Deb, J. Phys. B: At. Mol. Opt. Phys. **51**, 015004 (2018).

[18] J. D. Rodrigues, L. G. Marcassa, and J. T. Mendonça, J. Phys. B: At. Mol. Opt. Phys. **49**, 074007 (2018).

[19] B. Knuffman and G. Raithel, Phys. Rev. A **75**, 053401 (2007).

[20] K. R. Moore, S. E. Anderson, and G. Raithel, Nat. Commun. **6**, 6090 (2015).

[21] W. Petrich, M. H. Anderson, J. R. Ensher, and E. A. Cornell, Phys. Rev. Lett. **74**, 3352 (1995).

[22] L. Allen, M. W. Beijersbergen, R. J. C. Spreeuw, and J. P. Woerdman, Phys. Rev. A **45**, 8185 (1992).

[23] M. Mirhosseini, O. S. Magaña-Loaiza, C. Chen, B. Rodenburg, M. Malik, and R. W. Boyd, Opt. Express **21**, 30196 (2013).

[24] V. S. Malinovsky and J. L. Krause, Eur. Phys. J. D **14**, 147 (2001).

[25] T. F. Gallagher, *Rydberg Atoms* (Cambridge University Press, Cambridge, England, 1994).

[26] J. R. Rubbmark, M. M. Kash, M. G. Littman, and D. Kleppner, Phys. Rev. A **23**, 3107 (1981).

[27] P. R. Berman and V. S. Malinovsky, *Principles of Laser Spectroscopy and Quantum Optics* (Princeton University Press, Princeton, New Jersey, 2011).

[28] C. Zener, Proc. R. Soc. London Ser. A **137**, 696 (1932).

[29] E. K. Dietsche, A. Larrouy, S. Haroche, J. M. Raimond, M. Brune, and S. Gleyzes, Nat. Phys. **15**, 326 (2019).

[30] H. Labuhn, D. Barredo, S. Ravets, S. de Léséleuc, T. Marcí, T. Lahaye, and A. Browaeys, Nature **534**, 667 (2016).

[31] H. Bernien, S. Schwartz, A. Keesling, H. Levine, A. Omran, H. Pichler, S. Choi, A. S. Zibrov, M. Endres, M. Greiner *et al.*, Nature **551**, 579 (2017).

[32] J. Han, T. Vogt, C. Gross, D. Jaksch, M. Kiffner, and W. Li, Phys. Rev. Lett. **120**, 093201 (2018).

[33] M. M. Aliyu, A. Ulugöl, G. Abumwis, and S. Wüster, Phys. Rev. A **98**, 043602 (2018).

[34] D. W. Schumacher, J. H. Hoogenraad, D. Pinkos, and P. H. Bucksbaum, Phys. Rev. A **52**, 4719 (1995).